Sensors & Actuators: A. Physical 362 (2023) 114637

Contents lists available at ScienceDirect

Sensors and Actuators: A. Physical

journal homepage: www.journals.elsevier.com/sensors-and-actuators-a-physical

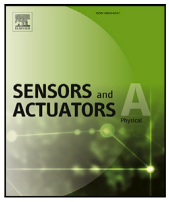

Aluminum nitride surface acoustic wave resonators with high Qf product by optical lithography

MinHee Kwon [a,*], Ioan Ignat [a], Daniel Platz [a], Holger Arthaber [b], Ulrich Schmid [a]

[a] Institute of Sensor and Actuator Systems, Technische Universität Wien, 1040 Vienna, Austria
[b] Institute of Electrodynamics, Microwave and Circuit Engineering, Technische Universität Wien, 1040 Vienna, Austria

ARTICLE INFO

Keywords:
Surface acoustic waves (SAW)
Aluminum nitride (AlN)
Resonator
Resonance frequency
Quality factor
Lithography
Butterworth-Van Dyke (BVD) equivalent circuit model

ABSTRACT

Surface acoustic wave (SAW) based devices have been developed in various fields such as for sensing applications. Even more, SAWs are recently studied in interaction with quantum systems, requiring high frequencies and high quality factors (Q factors). Here, we present single-port SAW resonators with resonance frequency above 1 GHz by depositing a layer of piezoelectric material with high phase velocity and designing the fine structure of an interdigital transducer (IDT). In detail, we fabricate SAW resonators on a sputtered aluminum nitride (AlN) layer with IDT finger size of 1 μm by photo-lithography. The devices are characterized by a vector network analyzer, operating at a resonance frequency up to 1.229 GHz with a quality factor Q of 2535 in air. The Q factors are analyzed as equivalent-circuit elements, thus separating external (Q_e) and internal (Q_i) quality factors. The analysis shows that the external quality factor Q_e can more straightforwardly be tuned by design parameters than the internal quality factor Q_i. The GHz resonance frequencies and internal quality factors above 1000 can be achieved even without the use of electron beam lithography.

1. Introduction

Surface acoustic wave (SAW) resonators were conceived in the early 1990s [1,2]. Such SAW resonators are formed by an interdigital transducer (IDT) for signal transduction and acoustic wave reflectors for spatially confining the SAWs. Different variants of SAW resonators have been developed since their invention. A particularly important design is the single-port resonator as schematically shown in Fig. 1. A single-port SAW resonator comprises two reflectors and one IDT on a piezoelectric substrate. The IDT is in most cases a periodic sequence of metal electrodes with transverse width W and an electrode width of p. The ratio of the electrode width p and the distance a between electrodes determines the metallization ratio which is commonly equal to 0.5. The wavelength λ is determined by the period of the IDT fingers, $\lambda = 2(p + a)$. Reflectors, distributed Bragg mirrors, are formed by large arrays of metal strips. The distance between the arrays and the IDT is d_s. SAWs are excited by an AC voltage which is applied to one part of IDT as shown in Fig. 1. When an electric field is generated between adjacent electrodes with different electric potentials, the piezoelectric effect creates a distortion of the piezoelectric material, and elastic waves are generated that propagate into both transverse directions of the IDT fingers [3]. On the other hand, the SAW is converted back into an electrical signal by the inverse piezoelectric effect when an elastic wave reflected by the mirror arrays reaches the IDT. If the electrode width of the reflector and the IDT are equal, the resonance frequency of the resonator is given by

$$f_0 = \frac{v_{\mathrm{SAW}}}{\lambda}, \tag{1}$$

where the phase velocity of waves v_{SAW} depends on the material in which the SAW propagates.

Single-port SAW resonators are utilized in a variety of applications like sensors for temperature, pressure, and gas [4,5]. Recently, hybrid quantum systems emerged as a new application for SAW technology. For example, it has been demonstrated that SAWs interact coherently with various quantum systems such as qubits [6–9]. Quantum applications require high SAW frequencies above 1 GHz. For such frequencies, the thermal quantum ground state of SAW resonators can be reached in modern cryostats. Besides, the quality factor (Q factor) of a resonator is another important key parameter for quantum applications since it determines the resonator's decoherence rate. High-Q factor resonators for quantum information processing have already been implemented using microelectromechanical system (MEMS) technology [10–14]. Although SAW resonators are fabricated using similar processes as silicon MEMS resonators, reaching high Q factors in SAW resonators with gigahertz frequencies remains challenging. Though SAW resonators with high-quality factors ($Q > 10^4$) have been demonstrated in the hundreds

* Corresponding author.
E-mail address: minhee.kwon@tuwien.ac.at (M. Kwon).

https://doi.org/10.1016/j.sna.2023.114637
Received 8 March 2023; Received in revised form 10 August 2023; Accepted 1 September 2023
Available online 22 September 2023

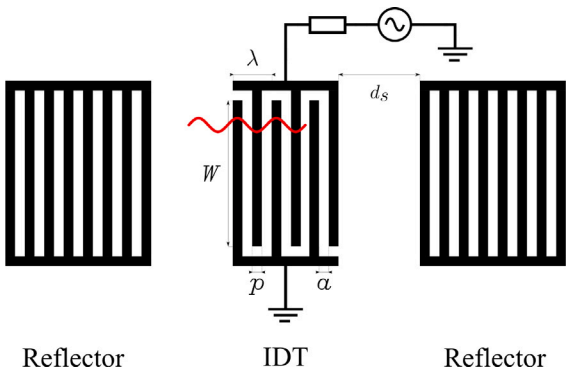

Fig. 1. Schematic diagram of the single-port surface acoustic wave (SAW) resonator. An IDT is in the center of the resonator, and reflectors are located symmetrically on both sides. The main geometry parameters of the resonator are the electrode width p, the spacing between the electrodes a, the transverse width of the electrodes W, and the distance between the IDT and the reflectors d_s. The length of a pair of IDT fingers is the wavelength λ of the SAW. One part of the IDT is connected to the ground, and the other part is connected to the AC signal.

of megahertz regimes on gallium arsenide (GaAs) [15] and in the gigahertz regime on ST-X quartz at 10 mK [16].

Sensor applications target the reduction of thermal noise in mechanical resonators for enhanced sensitivity. The thermal noise in a resonator is given by its thermal energy $\frac{1}{2}k_BT$ as stated by the equipartition theorem. This implies that decreasing the temperature reduces the thermal noise. Today, it is possible to reduce the temperature to a regime where quantum effects become relevant. In the quantum regime, the thermal energy is often characterized by the mean thermal occupancy $\langle\hat{n}\rangle$ of the resonator. The dependency of the mean thermal occupancy $\langle\hat{n}\rangle$ at the temperature T and the resonance frequency ω_0 is described by Bose–Einstein statistic

$$\langle\hat{n}\rangle = \left[\exp\left(\frac{\hbar\omega_0}{k_BT}\right) - 1\right]^{-1}, \tag{2}$$

where Boltzmann's constant k_B is 1.381×10^{-23} m^2 kg s^{-1} K^{-1}. At room temperature, a mean thermal occupancy $\langle\hat{n}\rangle$ below on requires resonance frequencies in the terahertz regime. This is naturally achieved for optical systems but not feasible for mechanical systems today. However, Eq. (2) implies that a mean thermal occupancy $\langle\hat{n}\rangle$ below one is also reached for resonance frequencies above 1 GHz at a temperature of 10 mK which are routinely reached in modern cryostat [16]. Thus, GHz SAW resonators are attractive candidates for future sensing applications with high sensitivity. Due to this outstanding feature, SAW structures operating at GHz are targeted as integrated components of a cantilevered sensor device offering reduced thermal noise levels such as needed in atomic force microscopy applications. While these results show that SAW resonators can be used in quantum applications, their fabrication is challenging. In most proof-of-concept experiments, the requirement of high SAW frequencies demands the use of advanced fabrication methods like electron beam lithography. Such fabrication methods are unsuitable for the mass production of devices and the large-scale deployment of quantum technologies. SAW-based devices fabricated using more established lithography processes like optical photo-lithography are much more desired for real-world applications.

Eq. (1) reveals that high frequencies are achieved not only by minimizing the SAW wavelength. Instead, a higher phase velocity also yields a higher SAW frequency at a given wavelength. The minimum wavelength is given by the lithography process while the phase velocity is a property of the piezoelectric material. Piezoelectric materials that are commonly used in quantum applications are for example zinc oxide (ZnO) [17], lithium niobate $LiNbO_3$ [18], ST-X quartz [16], or gallium arsenide (GaAs) [15]. These materials exhibit phase velocities between 2700 and 4000 m s^{-1} [15,19,20]. A material with a higher phase velocity of 5760 m s^{-1} is aluminum nitride (AlN) [21]. This phase velocity allows for reaching resonance frequencies above 1 GHz in an SAW resonator with SAW wavelengths of 4 µm. For such wavelengths, the fabrication of the resonator's IDT and Bragg mirrors does not require electron beam lithography [22]. Another advantage of AlN is that it is compatible with complementary metal–oxide–semiconductor (CMOS) technology [23], making AlN suitable for fabrication processes at semiconductor foundries. Much higher phase velocities such as above 6000 m s^{-1} can be obtained by depositing AlN on high-performance materials such as diamond [24], polyethylene naphthalate (PEN) [25], and aluminiumoxid (Al_2O_3) [26]. In the latter studies, SAWs by using standard photolithography are reported which are operated in the GHz regime.

In this paper, SAW resonators are fabricated on $LiNbO_3$ and AlN, respectively, and the phase velocity of the two materials is obtained to show that AlN is a suitable material for high-frequency resonators. We exploit the high SAW phase velocity in AlN and successfully demonstrate that AlN SAW resonators fabricated on pure silicon wafers using standard optical photo-lithography reach resonance frequencies above 1 GHz. Furthermore, we show that quality factors above 1000 are achieved in air at room temperature.

2. Experimental methods

2.1. Fabrication

Fig. 2 shows the fabrication process for the SAW resonators. We start from a pure high-resistivity silicon (Si) wafer with a bulk-resistivity higher than 10 000 Ω cm. We sputter-deposit an AlN layer on the Si wafer at a chamber pressure of 2 µbar under pure nitrogen atmosphere with a constant flow rate of 50 sccm, a plasma power of 800 W, and a substrate target distance of 65 mm. These sputter deposition parameters we used are such that AlN films can be deposited with a high degree of c-axis orientation, as reported in [27]. The AlN thin film has a thickness of 1 µm. AlN synthesized in a similar deposition process has piezoelectric coefficients d_{33} of 3.15 pm V^{-1} and d_{31} of 1.28 pm V^{-1} at a film thickness which is larger than 100 nm [28].

For patterning the IDT and the reflectors, we use a lift-off process that is based on a negative resist (AZ5214) as a sacrificial layer. We found that structuring small features down to 1 µm using conventional optical photo-lithography requires a thin layer of photoresist with a thickness of 650 nm. To achieve such a thin layer we dilute the photoresist in PGMEA and spin-coat it on top of the AlN layer. Next, we structure the photoresist layer by UV exposing it to the inverse pattern of the IDT and the reflectors. We flood UV-expose the complete resist film and develop it. On the developed film, we evaporate a layer of aluminum (Al) with a thickness of 150 nm and a capping layer of gold (Au) with a thickness of 10 nm to avoid oxidation of the aluminum. Because of the low mass loading effect, the Al-electrodes support high resonance frequency of an SAW [15,29,30]. We perform a lift-off process for the Al and Au layer by dipping the wafer in acetone and rinsing it. In the last step, the devices are separated with a wafer saw.

A false-color scanning electron microscopy (SEM) image of an example device fabricated using the described process is shown in Fig. 3(a). The device has an area of 3.7 mm by 2.0 mm. The IDT (purple) with 20 electrode pairs is located in the center of the device. The reflectors (green) are placed 500 µm away from the IDT and consist of 150 aluminum gratings. The smallest feature size we achieved with the process described above is 1 µm. Fig. 3(b) zooms into the IDT demonstrating this feature size as a homogeneous electrode width of 1 µm for all fingers in the IDT. The electrode width corresponds to an SAW wavelength of 4 µm.

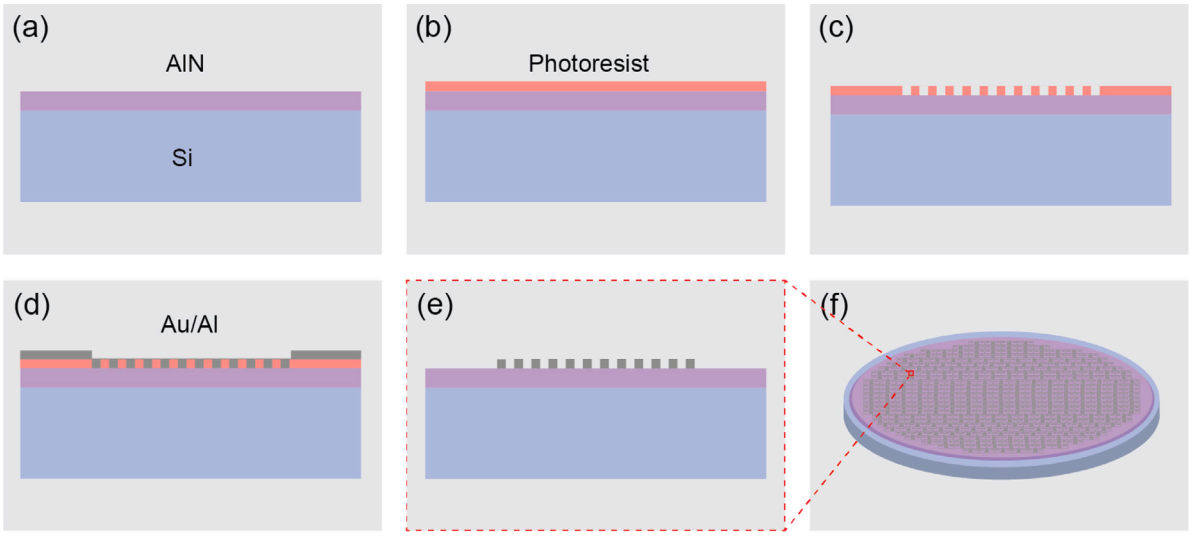

Fig. 2. Schematics of the fabrication process for the SAW resonators. (a) Sputter-deposition of AlN on Si wafer. (b) Deposition of photoresist by using spin-coater. (c) Exposure and development process by photo-lithography technology. (d) Metalization of Au/Al. (e) Lift-off by removing the photoresist layer. (f) Entire wafer after step (a)–(e). Chip dicing process is needed.

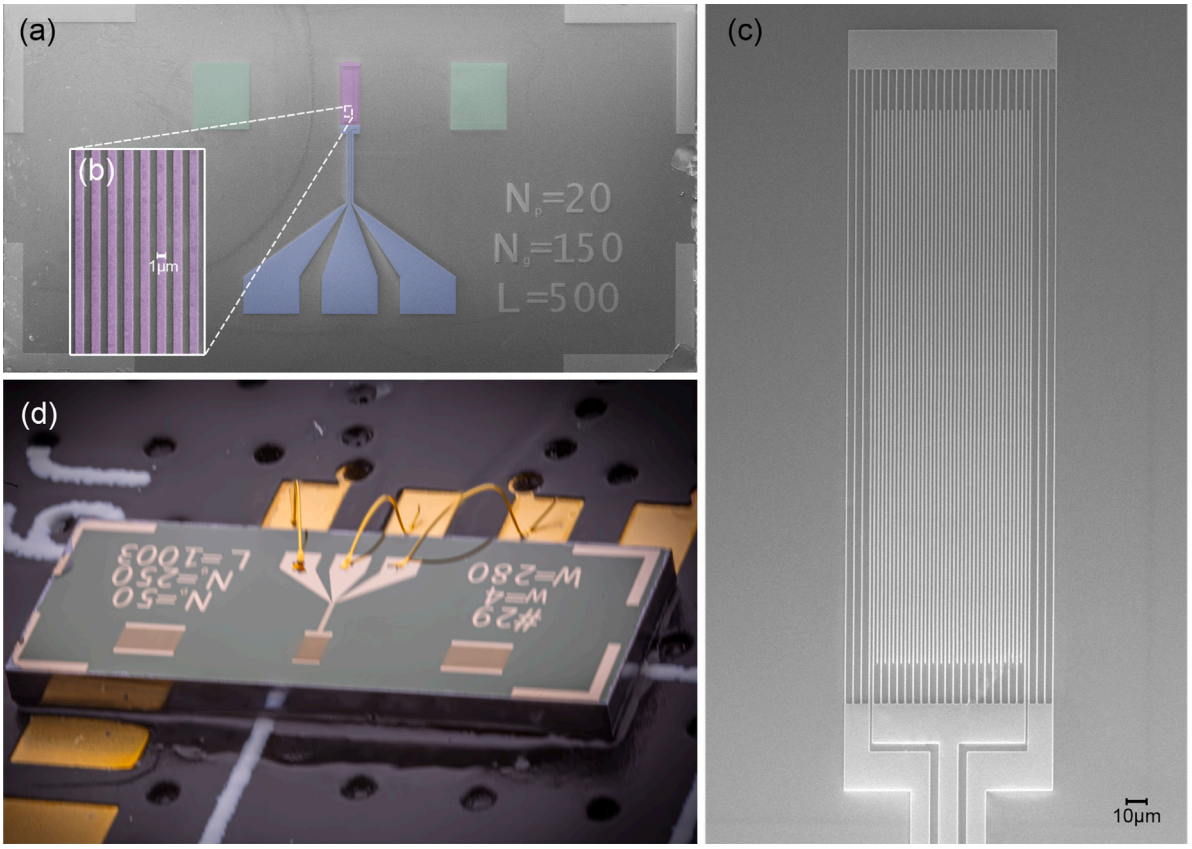

Fig. 3. (a) Scanning electron microscopy (SEM) image of the fabricated SAW resonator in false color. The purple-colored IDT is located in the center of the device, with green-colored reflectors placed on either side. The blue-colored pads are designed for coplanar waveguide (CPW) transmission line technology. The center pad is representing the signal path, and the two pads on either side are connected to the ground. The device size is 3.7 mm in width and 2 mm in height. (b) Zoomed-in SEM image of the electrodes of IDT with a size of electrode and spacing of 1 μm. (c) SEM image of the IDT in (a) with 20 pairs of electrodes. Additional electrodes are brought down from one busbar and connected to the CPW line. (d) The placed SAW device on the PC-board and wire-bonding between the device and PC-board. (For interpretation of the references to color in this figure legend, the reader is referred to the web version of this article.)

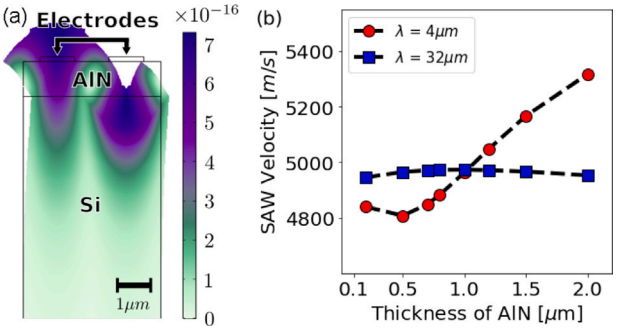

Fig. 4. (a) Simulated SAW mode with the colored map showing total displacement at eigenfrequency of 1.24 GHz. (b) Dependence of simulated phase velocity on the thickness of the AlN layer. The wavelengths of SAWs λ are 4 and 32 μm.

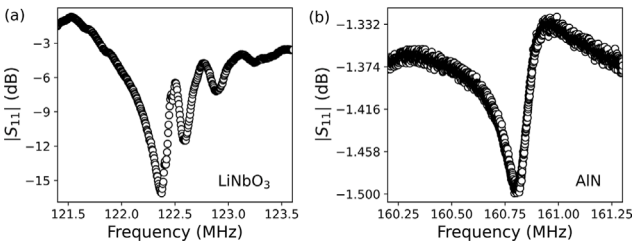

Fig. 5. (a) The magnitude of reflection coefficient S_{11} from manufactured SAW resonator on $LiNbO_3$ substrate and (b) on AlN/Si substrate.

2.2. Electrical characterization

We characterize the fabricated device with reflection measurements using a vector network analyzer (VNA, Rohde & Schwarz ZVL-6). For connecting the IDT port with the measurement setup, the device design includes coplanar waveguides (CPW) with a characteristic impedance of 50 Ω as shown in Fig. 3(a) in blue. Fig. 3(c) shows how the IDT and the CPW with pads are connected. The transducer has additional electrodes from one busbar of the IDT for a better electrical signal to ground pads. The structure of an ideal IDT is formed by two interlocking electrodes with different electrical poles. As shown in Fig. 3(c), the IDT has additional electrodes electrically connected to the ground, rather than a structure in which only pairs of fingers with different electrical poles are regularly arranged. This is because our IDT of the SAW resonators has an asymmetric design and this may have caused a loss in the connection path.

The CPW leads to aluminum electrode pads which are fabricated in the same photo-lithography process steps as the IDT. The devices are glued onto a custom-made printed circuit board (PCB) which is connected to the devices by gold wire bonding as shown in Fig. 3(d). The transmission lines on the PCB are designed for a characteristic impedance of 50 Ω and end in SubMiniature version A (SMA) connectors for connecting to the VNA. The VNA and the cable with the SMA connector were calibrated using a calibration kit (Rohde & Schwarz ZN-Z135). We used a full one-port calibration as in the short-open-match measurement for reflection measurements. With the VNA, we measure the reflection coefficient S_{11} of the devices as a function of frequency in air at room temperature.

3. Result and discussion

3.1. SAW phase velocity measurements

Eq. (1) contains two factors that affect the frequency f_0 of the SAW. The first is the wavelength λ of the SAW which is determined by the electrode width p of the IDT. The second is the phase velocity v_{SAW}, a parameter related to the material in which the SAW propagates. We study the SAW phase velocities by performing finite element method (FEM) simulations with COMSOL Multiphysics. The devices are then fabricated and measured to ensure that it matches the simulated values.

The 2D geometry of FEM simulation is shown in Fig. 4(a). It corresponds to the cross-section of the SAW device and comprises a pair of IDT electrodes on the AlN layer that is arranged on a Si substrate. The width of the 2D geometry is designed to match a single wavelength λ of the SAW and the thickness of the Si layer is 350 μm, which is the same as the Si wafer used. The width of each electrode on the AlN layer corresponds to the width p shown in Fig. 1. The material of the electrodes is Al and their thickness is 150 nm. We assume periodic boundary conditions to approximate the behavior of an IDT structure with a large number of electrode pairs. To determine the resonance frequency f_0, we perform an eigenfrequency analysis of the FEM model for different thicknesses of the AlN layer. Inserting the simulated eigenfrequencies into Eq. (1) together with the wavelength λ, that is defined by the IDT electrode width p, gives the phase velocity v_{SAW}.

To experimentally verify the simulated SAW phase velocity values, we fabricate the SAW resonators and measure their resonance frequency. We choose an electrode size for both IDT fingers and reflector gratings of $p = 8$ μm to achieve resonance frequencies in the megahertz regime while not working at the limits of the fabrication process. The width of the resonators is $W = 1600$ μm. The electrodes consist of a 150 nm thick layer of Al and a 10 nm capping layer of Au as described above. We compare AlN with $LiNbO_3$, which is another commonly used piezoelectric material for SAW devices, by fabricating the resonators on AlN and $LiNbO_3$ substrates. The $LiNbO_3$ substrate has a orientation of 128° Y-X cut with a thickness of 500 μm.

The resonance frequencies of the resonators are determined by the frequency minimum in the measured magnitude of the S_{11} reflection coefficient. Typical measurement results for both AlN and $LiNbO_3$ are shown in Fig. 5(a) and (b). The $LiNbO_3$ resonators exhibit a pronounced minima at $f_{LiNbO_3} = 122$ MHz with a depth of 1 dB. Besides the main resonance, three additional minima of smaller depth are visible in the S_{11} spectrum. For the AlN resonators, the depth of the S_{11} is only 0.25 dB deep but it is still clearly visible. The minimum is located at a frequency of $f_{AlN} = 161$ MHz. Using Eq. (1), we determine an SAW phase velocity of 3904 m s^{-1} for the $LiNbO_3$ resonators and a phase velocity of 5152 m s^{-1} for the AlN resonators. In the FEM simulation, a phase velocity of 4973 m s^{-1} was obtained for an AlN/Si substrate as shown in Fig. 4(b). We performed additional simulations for a $LiNbO_3$ substrate and obtained simulated phase velocity of 3738 m s^{-1} which is in good agreement with the measured phase velocity. AlN has higher phase velocities than $LiNbO_3$ with the same wavelength of SAWs at approximately 20 °C.

3.2. Thickness of the AlN layer

In a multilayered thin-film device, the SAW might propagate not only in the top layer of the device but might also penetrate into the materials arranged beneath the top layer. The phase velocities of the AlN on the Si wafer are lower than the phase velocity of pure AlN as 5760 m s^{-1} [21,26]. In this situation, the phase velocity differs from the phase velocity in a device comprising only one material. We study this dependency of the SAW phase velocity on the thickness of the AlN layer by FEM simulations.

Fig. 4(b) shows the simulated phase velocities for different AlN layer thicknesses between 0.1 μm and 2 μm. In the simulation, we consider wavelengths λ of 4 μm and 32 μm to investigate two different resonance frequencies. The wavelength of 32 μm results in a resonance frequency of hundreds of megahertz while for the wavelength of 4 μm the resonance frequency is higher than 1 GHz. For the wavelength of 4 μm,

the phase velocity increases from 4807 m s^{-1} at 0.5 μm to 5316 m s^{-1} at 2.0 μm as the thickness of the AlN layer increases. In contrast, the phase velocity for the wavelength of 32 μm is nearly independent of the AlN thickness, and its value is approximately 5000 m s^{-1}. The reason for this phase velocity is that the considered AlN thicknesses are relatively small compared to the wavelength of 32 μm.

The simulation results indicate that a larger thickness of AlN increases the SAW frequency, especially the wavelength of 4 μm. However, gigahertz frequencies are already reached at the AlN thickness of 1 μm. An example is shown in Fig. 4(a) where the wavelength is 4 μm and the AlN thickness is 1 μm. The color map indicates the displacement of the SAW mode at 1.24 GHz. The calculated phase velocity is 4963 m s^{-1}. Larger thicknesses of AlN deposition yield higher frequencies. However, the increase in frequencies is relatively small and requires a longer sputter-deposition time. Therefore, we choose the thickness of 1 μm in our fabrication process for devices with frequencies above 1 GHz.

3.3. Electrode width and resonance frequencies

The high SAW phase velocity on AlN substrates allows for the fabrication of SAW resonators with larger resonance frequencies compared to those with the same geometry parameters on other piezoelectric substrates. We explore the resonance frequency range in AlN resonators by fabricating resonators with different electrode width sizes of IDT and reflectors. The fabricated resonator feature electrode widths of 8 μm, 4 μm, 3 μm, and 1 μm. These values correspond to SAW wavelength of 32 μm, 16 μm, 12 μm, and 4 μm, respectively. The thickness of the AlN layer is 1 μm for all resonators. The other design parameters are described in Table 1.

The geometric parameters were considered and designed with previously reported SAW devices such as N_p of between 10 to 200, N_g of 100 or above, and W of length longer than 50 times the wavelength [6,15–17]. When the number of electrodes of the reflector N_g is more than 250, it is challenging to maintain the high geometrical precision which is the pattern of repeated rod-shaped metal structure, especially with a width of 1 μm, in the lift-off process. Thus, devices with more than 250 electrodes were not designed.

Fig. 6(a)–(d) displays the magnitude (red) and the phase (blue) of the measured complex S_{11} parameter as a function of frequency. All plots are centered around the main resonance of the resonator. The depth of the S_{11} minimum ranges from 0.1 dB to 2.1 dB. The S_{11} phase shift on resonance never exceeds 30° indicating that the devices are undercoupled to the VNA due to the small number of IDT fingers.

The measured resonance frequencies of the devices are 1.2287 GHz, 0.421 98 GHz, 0.319 63 GHz, and 0.160 840 GHz for wavelengths of 4 μm, 12 μm, 16 μm, and 32 μm, respectively. Fig. 6(e) shows that the measured resonance frequencies and phase velocities agree well with simulations. However, we find that for wavelengths above $\lambda = 12$ μm the error of SAW phase velocity is about 3.30%. These values agree with other theoretical predictions in literature [26]. Fig. 6(f) shows in principle the same data as Fig. 6(e), but for Fig. 6(f) the measured frequency has been converted into the corresponding phase velocities using Eq. (1). Therefore, the differences between experimental and simulated data in Fig. 6(f) are not larger than in Fig. 6(e). This impression might be due to the changed scale of the y-axis between Fig. 6(e) and (f).

3.4. Quality factors

The quality factor of a resonator is another important key parameter for various applications. We analyze the quality factor of the fabricated resonators by assuming two dominating loss mechanisms such that the total quality factor of the resonator is given by

$$\frac{1}{Q} = \frac{1}{Q_e} + \frac{1}{Q_i}. \tag{3}$$

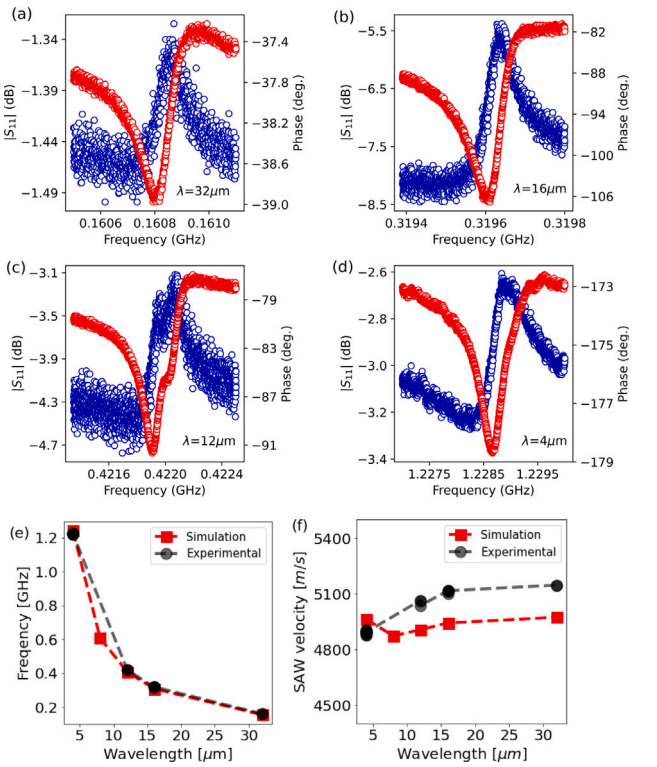

Fig. 6. (a)–(d) Measured reflection coefficient S_{11} of SAW resonators on AlN layer of 1 μm with wavelength λ of (a) 32, (b) 16, (c) 12, (d) 4 μm. Red and blue circles are the magnitude and phase of S_{11} respectively. (e)–(f) Dependence of (e) the resonance frequency and (f) phase velocity on the wavelength of SAWs. Red squares and black circles are the simulated and experimental data. (For interpretation of the references to color in this figure legend, the reader is referred to the web version of this article.)

Table 1
Geometrical parameters of four SAW resonators from Fig. 6: wavelength of an SAW λ, width of an IDT and grating electrodes p, number of IDT electrode pairs N_p, number of grating electrodes N_g, width of an transverse IDT-electrode W, distance between IDT and grating d_s.

λ [μm]	p [μm]	N_p	N_g	W [μm]	d_s [μm]	W/λ	d_s/λ
32	8	20	250	1600	1000	50	31
16	4	70	250	1000	500	63	31
12	3	20	250	1000	500	83	42
4	1	50	250	280	500	70	125

The external quality factor Q_e is a measure of coupling efficiency to external circuitry. The internal quality factor Q_i represents the total energy losses in the resonator itself, such as grating or diffraction losses. To determine the internal and the external quality factors from the measured S_{11} data, we model the single-port SAW resonator with the Butterworth–Van Dyke (BVD) equivalent circuit model in a transmission line with the characteristic impedance Z_0, as shown in Fig. 7 [31,32]. The equivalent circuit compromise the parallel static capacitance C_S of the IDT, the motional resistance R_M, the motional inductance L_M, and the motional capacitance C_M.

The scattering parameter for a single-port network, the reflection coefficient S_{11}, can be calculated in terms of the impedances in Fig. 7 by the equation,

$$S_{11} = \frac{Z - Z_0}{Z + Z_0}, \tag{4}$$

where Z is the impedance of the resonator of the BVD model with a port of impedance Z_0 [32]. In this model, the reflection coefficient S_{11} of Eq. (4) can be expressed in terms of the internal quality factor Q_i and the external quality factor Q_e as

Table 2
Benchmark of Qf product of the AlN-based resonators on silicon wafers.

Parameter [units]	This work	[26]	[34]	[35]	[36]
Substrate [-]	Si	Si	Si-SiO_2-Si	Si-SiO_2-Si	SiO_2-Si
Resonance frequency f_0 [MHz]	1229.2	700	496	208	427
Quality factor Q [-]	2535	1300	3800	6100	1400
Qf product ($f_0 \times Q$) [10^{12}·Hz]	3.1	0.9	0.2	1.3	0.6

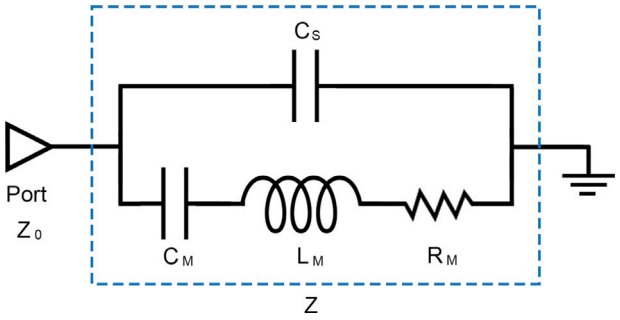

Fig. 7. The simple Butterworth–Van Dyke (BVD) equivalent circuit model of a piezoelectric resonator in the transmission line of characteristic impedance Z_0 [31,32]. The BVD model consists of the static capacitance C_S and the branch of the motional resistance R_M, the inductance L_M, and the capacitance C_M.

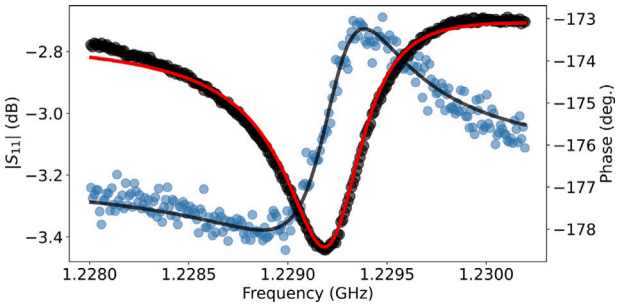

Fig. 8. Measured reflection coefficient S_{11} of the SAW resonator with the wavelength of 4 μm in the gigahertz regime. Black and blue circles are the magnitude and phase of S_{11} respectively, and the solid line is the fitting curve from Eq. (5). (For interpretation of the references to color in this figure legend, the reader is referred to the web version of this article.)

$$S_{11}(f) = \frac{(Q_e - Q_i)/Q_e + i(2Q_i(f - f_0))/f_0}{(Q_e + Q_i)/Q_e + i(2Q_i(f - f_0))/f_0} \tag{5}$$

[15,16,32,33]. It should be noted that S_{11} in this equation is complex. As a consequence, a fit of only the S_{11} magnitude does not suffice to uniquely determine the internal and external quality factors. We thus fit the magnitude and phase data at the same time.

Fig. 8 shows a typical example demonstrating the good agreement between the fitted function and the measured data with the geometry parameters, $a = 1\,\mu m$, $W = 280\,\mu m$, $d_s = 500\,\mu m$, $N_p = 50$ and $N_g = 250$ on a thin AlN film of 1 μm. Here, the resonance frequency f_0 of the resonator is 1.2292 GHz, while the external Q factor Q_e is 7027 and the internal Q factor Q_i is 3967. These values imply a $f \cdot Q$ product of 3.1160×10^{12} which is higher than the results of AlN-on-silicon resonators in air reported in literature [26,34–36] as shown in Table 2. The $f \cdot Q$ product values of the four devices as a function of the wavelength are shown in Fig. 9. Each of the four values is from the devices shown in Fig. 6.

The internal and external quality factors can be tuned by the design parameters of the resonators. Especially the number of IDT finger pairs N_p and the number of gratings N_g in the reflectors are key parameters for the Q factors [3,15]. More specifically, the external Q factor Q_e is given by

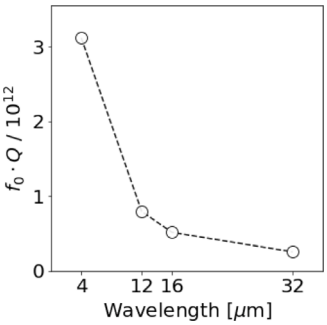

Fig. 9. $f \cdot Q$ product of the fabricated SAW resonators on AlN as a function of wavelength λ.

$$Q_e = \frac{L_c}{5.74 v_0 Z_c C_0 W K^2 {N_p}^2} \tag{6}$$

with effective resonator length L_c, wave propagation speed v_0, characteristic impedance of the electrical port coupled to the IDT $Z_c = 50\,\Omega$, effective dielectric constant C_0 and coupling coefficient K^2 [3,15]. The effective dielectric constant C_0 represents the capacitance per unit length of a single finger pair. C_0 is $0.50\,pF\,cm^{-1}$ by calculating with $C_0 = K(\varepsilon_{AlN} + 1)$ where the substrate dielectric constant ε_{AlN} and an empirical value K are 10 and 4.53, respectively [37,38]. The internal Q factor Q_i is the result of different damping mechanisms like diffraction losses, viscoelastic losses, or air damping. A major source of internal damping is grating losses which are due to non-perfect reflection at the grating reflectors. The Q factor Q_g corresponding to grating losses is given by

$$Q_g = \frac{\pi L_c}{\lambda_0(1 - \tanh(|r_s|N_g))} \tag{7}$$

where r_s is the single electrode reflectivity [3,15]. The value of r_s which is defined by the free spectral range (FSR $= 2f_0/\{(2d_s + \lambda N_p - a)/2a + 1/|r_s|\}$ [3,16]) from our device is approximately 0.008. As the Eq. (7), a larger number N_g of reflector gratings leads to a high grating loss quality factor Q_g due to an increase in the total reflections at the gratings. In contrast, a larger number N_p of IDT electrode pairs leads to a lower external quality factor since more acoustic energy can be extracted from the resonator by the external circuitry. Effective resonator length L_c, which is related to the distance between the IDT and the reflectors d_s, also affects the internal and external Q factors. In our designs, we chose a value for d_s that is 50 times larger than the SAW wavelength. This value is relatively large compared to resonator designs in which the reflector gratings are placed directly next to the IDT. Here, we wanted to SAW resonator to exhibit space for additional components like qubits in future research.

To investigate how strongly the total Q factor of the fabricated SAW resonators depends on these design parameters, we determine the internal and external Q factors from measured S_{11} data for a different number of IDT electrode pairs and reflector gratings, respectively. Fig. 10(a) shows the obtained external Q factor Q_e for N_p = 20, 50, 70, 100, 200 IDT electrode pairs and Fig. 10(b) shows the internal Q_g for N_g = 100, 150, 200 reflector gratings.

To evaluate how well the design parameters N_p and N_g predict the internal and external quality factor, we reduce Eqs. (6) and (7) to

$$Q_e = p_e \frac{1}{{N_p}^2}, \quad Q_g = \frac{p_i}{1 - \tanh(|r_s|N_g)} \tag{8}$$

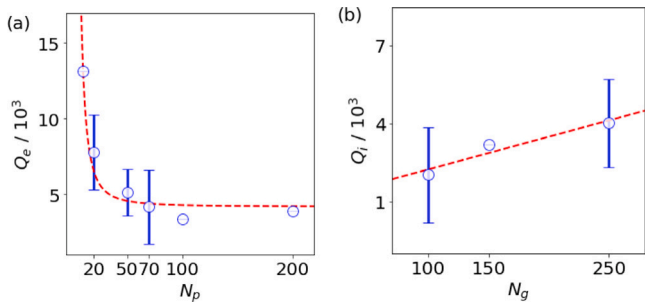

Fig. 10. (a) Measured external quality factor Q_e of SAW resonators as changes of number of IDT pairs N_p. The dashed line is the fitting curve from Eq. (8)Q_e. (b) Measured internal quality factor Q_i of SAW resonators as changes in the number of reflectors N_g. The dashed line is the fitting curve from Eq. (8)Q_g.

with the free fit parameters p_e and p_i. The results show that the external quality factor can be well controlled by the number N_p of IDT electrode pairs and below $N_p = 100$ the external quality factor rapidly increases with decreasing N_p. At $N_p = 20$ energy extraction becomes inefficient and the data show relatively large fluctuations between different devices. The dependency of the internal quality factor on the number N_g of reflector gratings is less pronounced. This indicates that other loss mechanisms than grating losses like air damping contribute significantly to the total internal quality factor. Though, the internal quality factor is well above 1000 for nearly all devices.

3.5. Impedance matching network

It is important that the impedance matching network is placed between a load and feed line for real-life applications [32]. In practical applications, an LC impedance matching adding of an inductor and a capacitor is a common practice for RF components. Inductors and capacitors are commonly used for impedance matching because they are tiny, inexpensive, and available with finely graduated scale values. Any impedance can be matched to 50 Ω by choosing an appropriate arrangement, for example, which elements are in parallel and which elements are in series.

The magnitude of reflection coefficient S_{11} of the SAW resonators we measured in Fig. 6(a)–(d) is about 1 dB. The SAW devices we investigated were not optimized for impedance matching to an external circuit. To study if the amplitudes and phase of S_{11} could be controlled by an improved impedance matching, we perform circuit simulations in AWR Design Environment's Microwave Office. In order to do so, we extend the circuit in AWR Design Environment simulations to design the impedance matching network by using a transformer and a phase shift instead of LC matching. The reason for using the transformer and phase shifter in the simulations is that the phase and magnitude of the S_{11} can be controlled independently. If L and C are added to the circuit respectively, tuning is more challenging because the phase and magnitude are linked with each other. Using a transformer and a phase shifter eliminates the need to change the circuit topology. For narrowband devices, the transformer and the phase shifter can always be replaced with an LC circuit and vice versa. In these simulations, the matching circuit comprises a transformer and a phase shifter as shown in Fig. 11(a) which are characterized by the turns ratio N and a phase shifting ϕ. The SAW part of the circuit is characterized by the measured reflection coefficient S_{11}. Next, we tune N and ϕ such that the device is matched at its resonance frequency.

The data used in the simulations is the same as the data shown in Fig. 8. Fig. 11(b) and (c) display the original measured response and the simulated response with optimized impedance matching. This circuit of Fig. 11(a) is characterized as a matching network with the turns ratio of a transformer N of 0.44 and phase shifting ϕ of 178.2°. Fig. 11(b)

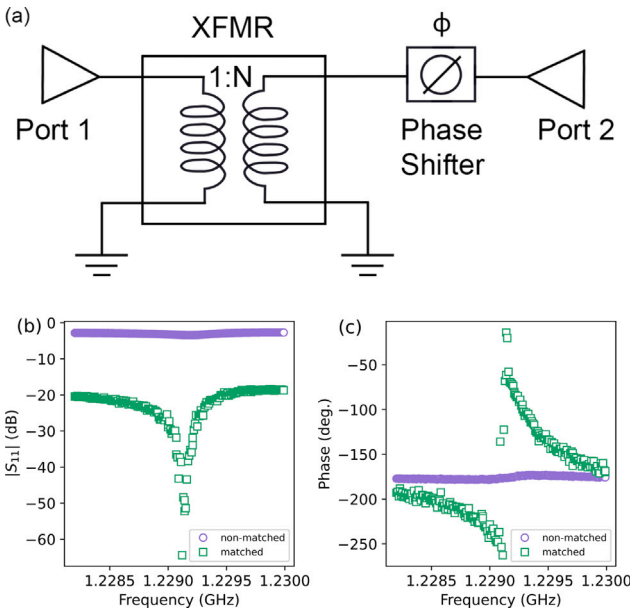

Fig. 11. (a) The circuit as a matching network with a transformer and phase shifter. The turns ratio of a transformer is N with a value of 0.44 and the phase-shifting angle ϕ is 178.2° determined from AWR Design Environment. In the simulation, port 1 has an impedance of 50 Ω, and port 2 is evaluated against the measured data. (b) The measured magnitude of reflection coefficient S_{11}. The purple circles are before impedance matching and the green squares are after impedance matching with a transformer and phase shifter. (c) The measured phase of reflection coefficient S_{11}. The purple circles are before impedance matching and the green squares are after impedance matching with a transformer and phase shifter. (For interpretation of the references to color in this figure legend, the reader is referred to the web version of this article.)

and (c) show the magnitude and phase of reflection coefficient S_{11} respectively. In Fig. 11(b), purple circles are data without the impedance matching network, and green squares are data with artificial impedance matching network at the resonance frequency of 1.2292 GHz. The phase shows that the difference between the highest and lowest value before matching is 5.52°, and the difference between the phases after matching is 248.59° shown in purple circles and green squares in Fig. 11(c). The analysis with the AWR Design Environment simulator indicates that the response of our devices increased by the impedance matching for real-life applications. There are other methods besides matching impedances to improve the characteristics of the SAW device, such as adjusting geometry parameters of SAW structures related to external losses or matching the feed line with characteristic impedance to a smaller than 50 Ω, such as 10 or 5 Ω.

3.6. Effect of bond wires

The SAW resonators are wire-bonded to PCBs. The inductance of the wires which connect the SAW devices with PCBs can cause losses. The inductance of a single round wire as 0.76 nH is calculated [39] with the wire's diameter of 25 μm and length of approximately 900 μm which is the average length measured with SEM. In order to analyze how much the inductance of the bond wires affects the reflection coefficient S_{11}, the BVD model of Fig. 7 is simulated in AWR Design Environment's Microwave Office.

The electrical characteristics of an SAW resonator are modeled by the modified BVD model for single-port measurement. In the simulations, the modified BVD model has an additional resistance R_A in series to the port with impedance Z_0 in the BVD model as we showed previously in Fig. 7. The modified BVD model by adding a series resistance R_A to the input port includes the electrical losses of the electrodes [40]. The equivalent circuit parameters from the AWR Design Environment

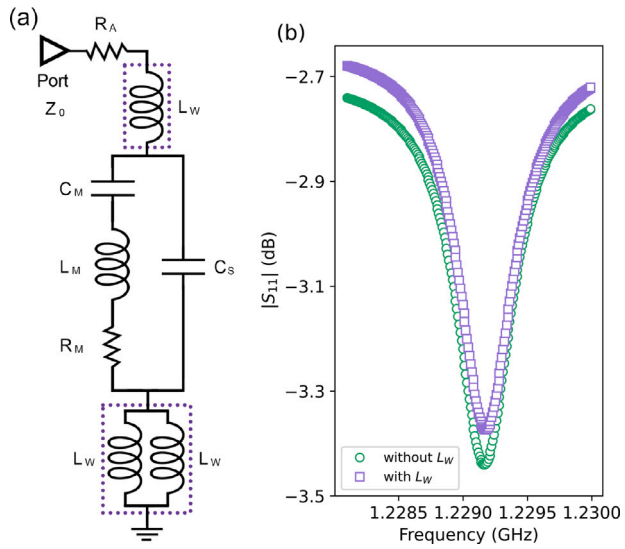

Fig. 12. (a) The circuit model with the inductances of the bond wire L_W, in the purple dotted boxes, to the modified Butterworth–Van Dyke (MBVD) model which adds a series resistance R_A from the simple BVD model shown in Fig. 7. As shown in Fig. 3(c) and (d), the IDT is connected to the ground by two electrode pads with wires. This means that two inductances L_W are connected in parallel with the ground in the BVD model circuit. (b) The simulated magnitude of reflection coefficient S_{11}. The green circles are from the MBVD model without the inductances L_W of the bond wire. The purple squares are from the circuit model of (a) with the inductances L_W of the bond wire. (For interpretation of the references to color in this figure legend, the reader is referred to the web version of this article.)

simulator are static capacitance C_S of 74.09 pF, the motional resistance R_M of 1.47 Ω, the motional inductance L_M of 0.47 μH, the motional capacitance C_M of 0.04 pF, and the additional resistance R_A of 7.71 Ω for the SAW resonator at 1.2292 GHz. The absolute values of reflection coefficient S_{11} of the modified BVD model with circuit parameters are represented by green circles in Fig. 12(b).

Fig. 12(a) shows the circuit in which the inductances of bond wire L_W are added to the input port including the ground of the modified BVD model for the AWR Design Environment simulator. The purple dotted boxes in Fig. 12(a) model only the bond wires which indicate one signal connection and two ground connections. In the simulation, the circuit parameters such as C_S, R_M, L_M, C_M, and R_A are the same as we used before, and the value of inductance of the bond wire L_W is 0.76 nH as calculated. A modified BVD model including inductances L_W has a reflection coefficient S_{11} shown in Fig. 12(b) as purple squares. Fig. 12(b) yields the effect of wire-bondings by simulating the modified BVD model. The minimum value of the S_{11} before adding the inductances of the wire L_W is −3.44 dB, and after adding inductances L_W the value is −3.37 dB, and the frequencies indicated by the minimum values of S_{11} are the same as 1.2292 GHz. The result of this simulation confirms that the losses of the SAW signals occur by inductances arising from the wire bonds. Although the effect of wire-bondings is not strong, to reduce the effect, connecting multiple wires between SAW devices and PCBs means that several inductances L_W, in the modified BVD model, are generated in parallel, so the total inductance value inside the purple dotted square is reduced in Fig. 12(a).

4. Conclusion

This paper reports on the fabrication of SAW resonators on AlN-on-silicon substrates with frequencies above 1 GHz. With the presented fabrication process, we achieve an IDT and grating electrode width size as small as 1 μm without the use of advanced lithography methods like electron beam lithography. This together with the high SAW phase velocity in AlN allows for reaching resonance frequencies up to 1.2292 GHz. Moreover, we find external quality factors of up to 9894 and internal quality factors of up to 5878 in air with the gigahertz response, while the value of the Qf product is as high as 3.1160×10^{12}. All in all, high quality SAW devices based on an AlN-on-silicon technology are demonstrated to have resonance frequencies above 1 GHz even when fabricated with optical lithography.

Declaration of competing interest

The authors declare that they have no known competing financial interests or personal relationships that could have appeared to influence the work reported in this paper.

Data availability

Data will be made available on request.

Acknowledgments

We would like to thank the QAFM team for insightful and detailed discussions on the topic: D.B. Haviland, E.K. Arvidsson, A.K. Roos, E. Scarano, E. Holmgren, T. Glatzel, and M. Zutter., from Intermodulation Products, E.A. Tholén and D. Forchheimer.

This project has received funding from the European Union's Horizon 2020 research and innovation programme under grant agreement No 828966 (https://cordis.europa.eu/project/id/828966).

The authors acknowledge TU Wien Bibliothek for financial support through its Open Access Funding Programme.

References

[1] W. Buff, SAW sensors, Sensors Actuators A 30 (1–2) (1992) 117–121, http://dx.doi.org/10.1016/0924-4247(92)80205-H.

[2] F. Seifert, W.-E. Bulst, C. Ruppel, Mechanical sensors based on surface acoustic waves, Sensors Actuators A 44 (3) (1994) 231–239, http://dx.doi.org/10.1016/0924-4247(94)00808-6.

[3] D. Morgan, Surface Acoustic Wave Filters: With Applications to Electronic Communications and Signal Processing, Academic Press, 2010.

[4] B. Liu, X. Chen, H. Cai, M.M. Ali, X. Tian, L. Tao, Y. Yang, T. Ren, Surface acoustic wave devices for sensor applications, J. Semicond. 37 (2) (2016) 021001, http://dx.doi.org/10.1088/1674-4926/37/2/021001.

[5] D. Mandal, S. Banerjee, Surface acoustic wave (SAW) sensors: Physics, materials, and applications, Sensors 22 (3) (2022) 820, http://dx.doi.org/10.3390/s22030820.

[6] M.V. Gustafsson, T. Aref, A.F. Kockum, M.K. Ekström, G. Johansson, P. Delsing, Propagating phonons coupled to an artificial atom, Science 346 (6206) (2014) 207–211, http://dx.doi.org/10.1126/science.1257219.

[7] B.A. Moores, L.R. Sletten, J.J. Viennot, K. Lehnert, Cavity quantum acoustic device in the multimode strong coupling regime, Phys. Rev. Lett. 120 (22) (2018) 227701, http://dx.doi.org/10.1103/PhysRevLett.120.227701.

[8] K.J. Satzinger, Y.P. Zhong, H.-S. Chang, G.A. Peairs, A. Bienfait, M.-H. Chou, A.Y. Cleland, C.R. Conner, É. Dumur, J. Grebel, I. Gutierrez, B.H. November, R.G. Povey, S.J. Whiteley, D.D. Awschalom, D.I. Schuster, A.N. Cleland, Quantum control of surface acoustic-wave phonons, Nature 563 (7733) (2018) 661–665, http://dx.doi.org/10.1038/s41586-018-0719-5.

[9] L. Sletten, B. Moores, J. Viennot, K. Lehnert, Resolving phonon fock states in a multimode cavity with a double-slit qubit, Phys. Rev. X 9 (2) (2019) 021056, http://dx.doi.org/10.1103/PhysRevX.9.021056.

[10] K. Yasumura, T. Stowe, E. Chow, T. Pfafman, T. Kenny, B. Stipe, D. Rugar, Quality factors in micron- and submicron-thick cantilevers, J. Microelectromech. Syst. 9 (1) (2000) 117–125, http://dx.doi.org/10.1109/84.825786.

[11] K.L. Ekinci, M.L. Roukes, Nanoelectromechanical systems, Rev. Sci. Instrum. 76 (6) (2005) 061101, http://dx.doi.org/10.1063/1.1927327.

[12] S.A. Chandorkar, M. Agarwal, R. Melamud, R.N. Candler, K.E. Goodson, T.W. Kenny, Limits of quality factor in bulk-mode micromechanical resonators, in: 2008 IEEE 21st International Conference on Micro Electro Mechanical Systems, IEEE, 2008, http://dx.doi.org/10.1109/MEMSYS.2008.4443596.

[13] W.J. Venstra, H.J.R. Westra, H.S.J. van der Zant, Q-factor control of a microcantilever by mechanical sideband excitation, Appl. Phys. Lett. 99 (15) (2011) 151904, http://dx.doi.org/10.1063/1.3650714.

[14] R. Abdolvand, B. Bahreyni, J. Lee, F. Nabki, Micromachined resonators: A review, Micromachines 7 (9) (2016) 160, http://dx.doi.org/10.3390/mi7090160.

[15] T. Aref, P. Delsing, M.K. Ekström, A.F. Kockum, M.V. Gustafsson, G. Johansson, P.J. Leek, E. Magnusson, R. Manenti, Quantum acoustics with surface acoustic waves, in: Superconducting Devices in Quantum Optics, Springer, 2016, pp. 217–244.

[16] R. Manenti, M. Peterer, A. Nersisyan, E. Magnusson, A. Patterson, P. Leek, Surface acoustic wave resonators in the quantum regime, Phys. Rev. B 93 (4) (2016) 041411, http://dx.doi.org/10.1103/PhysRevB.93.041411.

[17] L.L. Brizoual, F. Sarry, O. Elmazria, P. Alnot, S. Ballandras, T. Pastureaud, GHz frequency ZnO/Si SAW device, IEEE Trans. Ultrason. Ferroelectr. Freq. Control 55 (2) (2008) 442–450, http://dx.doi.org/10.1109/TUFFC.2008.662.

[18] L. Shao, S. Maity, L. Zheng, L. Wu, A. Shams-Ansari, Y.-I. Sohn, E. Puma, M. Gadalla, M. Zhang, C. Wang, E. Hu, K. Lai, M. Lončar, Phononic band structure engineering for high- iQ/i Gigahertz surface acoustic wave resonators on lithium niobate, Phys. Rev. A 12 (1) (2019) 014022, http://dx.doi.org/10.1103/PhysRevApplied.12.014022.

[19] A.J. Slobodnik, Surface acoustic waves and SAW materials, Proc. IEEE 64 (5) (1976) 581–595.

[20] Y. Fu, J. Luo, N. Nguyen, A. Walton, A. Flewitt, X. Zu, Y. Li, G. McHale, A. Matthews, E. Iborra, H. Du, W. Milne, Advances in piezoelectric thin films for acoustic biosensors, acoustofluidics and lab-on-chip applications, Prog. Mater. Sci. 89 (2017) 31–91, http://dx.doi.org/10.1016/j.pmatsci.2017.04.006.

[21] G. Bu, D. Ciplys, M. Shur, L.J. Schowalter, S. Schujman, R. Gaska, Surface acoustic wave velocity in single-crystal AlN substrates, IEEE Trans. Ultrason. Ferroelectr. Freq. Control 53 (1) (2006) 251–254, http://dx.doi.org/10.1109/TUFFC.2006.1588412.

[22] L. Kelly, H. Northfield, S. Rashid, X. Bao, P. Berini, Fabrication of high frequency SAW devices using tri-layer lift-off photolithography, Microelectron. Eng. 253 (2022) 111671, http://dx.doi.org/10.1016/j.mee.2021.111671.

[23] S. Trolier-McKinstry, P. Muralt, Thin film piezoelectrics for MEMS, J. Electroceram. 12 (1) (2004) 7–17.

[24] S. Fujii, High-frequency surface acoustic wave filter based on diamond thin film, Phys. Status Solidi a 208 (5) (2011) 1072–1077, http://dx.doi.org/10.1002/pssa.201000064.

[25] L. Lamanna, F. Rizzi, V.R. Bhethanabotla, M.D. Vittorio, GHz AlN-based multiple mode SAW temperature sensor fabricated on PEN substrate, Sensors Actuators A 315 (2020) 112268, http://dx.doi.org/10.1016/j.sna.2020.112268.

[26] C. Caliendo, P. Imperatori, High-frequency, high-sensitivity acoustic sensor implemented on ALN/Si substrate, Appl. Phys. Lett. 83 (8) (2003) 1641–1643, http://dx.doi.org/10.1063/1.1604482.

[27] M. Gillinger, M. Schneider, A. Bittner, P. Nicolay, U. Schmid, Impact of annealing temperature on the mechanical and electrical properties of sputtered aluminum nitride thin films, J. Appl. Phys. 117 (6) (2015) 065303, http://dx.doi.org/10.1063/1.4907208.

[28] A. Ababneh, M. Alsumady, H. Seidel, T. Manzaneque, J. Hernando-García, J. Sánchez-Rojas, A. Bittner, U. Schmid, C-axis orientation and piezoelectric coefficients of AlN thin films sputter-deposited on titanium bottom electrodes, Appl. Surf. Sci. 259 (2012) 59–65, http://dx.doi.org/10.1016/j.apsusc.2012.06.086.

[29] C. Campbell, Surface Acoustic Wave Devices for Mobile and Wireless Communications, Four-Volume Set, Academic Press, 1998.

[30] A. Muller, A. Nicoloiu, A. Dinescu, A. Stavrinidis, I. Zdru, G. Konstantinidis, The influence of metallization on resonance frequency and temperature sensitivity of GHz operating III-nitride SAW based sensor structures, in: 2018 IEEE/MTT-S International Microwave Symposium - IMS, IEEE, 2018, http://dx.doi.org/10.1109/MWSYM.2018.8439423.

[31] K.S. Van Dyke, The piezo-electric resonator and its equivalent network, Proc. Inst. Electron. Radio Eng. 16 (6) (1928) 742–764.

[32] D.M. Pozar, Microwave Engineering, John wiley & sons, 2011.

[33] G. Crupi, G. Gugliandolo, G. Campobello, N. Donato, Measurement-based extraction and analysis of a temperature-dependent equivalent-circuit model for a SAW resonator: From room down to cryogenic temperatures, IEEE Sensors J. 21 (10) (2021) 12202–12211, http://dx.doi.org/10.1109/JSEN.2021.3066345.

[34] H.M. Lavasani, R. Abdolvand, F. Ayazi, A 500MHz low phase-noise A1N-on-silicon reference oscillator, in: 2007 IEEE Custom Integrated Circuits Conference, IEEE, 2007, http://dx.doi.org/10.1109/CICC.2007.4405803.

[35] R. Abdolvand, H. Lavasani, G. Ho, F. Ayazi, Thin-film piezoelectric-on-silicon resonators for high-frequency reference oscillator applications, IEEE Trans. Ultrason. Ferroelectr. Freq. Control 55 (12) (2008) 2596–2606, http://dx.doi.org/10.1109/TUFFC.2008.976.

[36] H.M. Lavasani, W. Pan, F. Ayazi, An electronically temperature-compensated 427MHz low phase-noise AlN-on-Si micromechanical reference oscillator, in: 2010 IEEE Radio Frequency Integrated Circuits Symposium, IEEE, 2010, http://dx.doi.org/10.1109/RFIC.2010.5477392.

[37] M. Schneider, A. Bittner, U. Schmid, Impact of film thickness on the temperature-activated leakage current behavior of sputtered aluminum nitride thin films, Sensors Actuators A 224 (2015) 177–184, http://dx.doi.org/10.1016/j.sna.2015.01.032.

[38] G.W. Farnell, I.A. Cermak, P. Silvester, S. Wong, Capacitance and field distributions for interdigital surface-wave transducers, IEEE Trans. Sonics Ultrason. 17 (3) (1970) 188–195.

[39] B.C. Wadell, Transmission Line Design Handbook, Artech House Microwave Library, 1991.

[40] J. Larson, P. Bradley, S. Wartenberg, R. Ruby, Modified Butterworth-Van Dyke circuit for FBAR resonators and automated measurement system, in: 2000 IEEE Ultrasonics Symposium. Proceedings. an International Symposium (Cat. No.00CH37121), IEEE, 2000, http://dx.doi.org/10.1109/ULTSYM.2000.922679.